Nature Communications

https://doi.org/10.1038/s41467-026-69945-5

Article in Press

Chiral inheritance effect in the reactive cystine-based coassembly system

Received: 18 August 2025

Accepted: 13 February 2026

Cite this article as: Wang, Z., Chu, C., Hao, A. *et al.* Chiral inheritance effect in the reactive cystine-based coassembly system. *Nat Commun* (2026). https://doi.org/10.1038/s41467-026-69945-5

Zhuoer Wang, Changyu Chu, Aiyou Hao & Pengyao Xing

Chiral Inheritance Effect in the Reactive Cystine-Based Coassembly System

Zhuoer Wang,[1,†] Changyu Chu, [1,†] Aiyou Hao,[1] Pengyao Xing[1,*]

1.School of Chemistry and Chemical Engineering, Shandong University, Jinan 250100, P. R. China.

[†]*These authors contributed equally: Zhuoer Wang, Changyu Chu.*

**Corresponding author: xingpengyao@sdu.edu.cn*

Abstract

Controlled chemical reactions in the condensed state are key steps in designing smart materials. Due to the absence of diffusion and sufficient molecular collision, the reaction efficiency in the solid or aggregated state is expectedly much lower than the solution phase. Herein we report the templating effects in self-assemblies undergoing multiple reactions using an aromatic cystine derivative. Disulfide bond cleavage into cysteine triggered by a reductant is quantitative in aggregates, leading to the molecular rearrangement. Coassembled with a guest pentafluoropyridine through π-hole/π interaction allows for a cascade two step reaction including reduction and aromatic nucleophilic substitution. These reactions in the condensed, self-assembled state are efficient with significant impacts on the structures of nanoarchitectures. Interestingly, the chiral expression at macroscopic scale and corresponding chiroptical activities exhibit templating and inheritance effect thanks to the sacrificial templating role of pristine aggregates. We introduce new type efficient reactions in the self-assembled states, realizing flexible control by introducing guest, and unveil the chiral inheritance effect in topochemical evolutions.

Introduction

Materials composed of molecular units with intrinsic responsiveness can undergo reversible changes in chemical structure or molecular conformation upon exposure to external stimuli such as light, heat, electric field, pH, or chemicals.[1-6] These transformations can further induce macroscopic changes in color, morphology, swelling, conductivity, and luminescence.[7-13] Molecular and supramolecular systems are primarily engineered to respond to such stimuli, most of which rely on reversible non-covalent interactions under kinetic control, such as rapid interfacial adsorption.[14-19] However, stimuli-responsive materials governed by chemical reactions, particularly those operating under spatial confinement such as in the solid state, remain a significantly underexplored area. Their importance lies in the ability of such constrained environments to direct supramolecular assembly through spatial restrictions, thereby enabling unique chiroptical properties. In contrast to previously reported chiral nanostructures, these in situ transformation systems, prepared via a post-assembly reaction approach, exhibit a strong templating effect and promising potential for applications in adaptive optical devices, chiroptical switches, and smart sensors. Nonetheless, limitations such as slow response kinetics, limited recyclability, and challenges in precisely controlling and determining the exact molecular self-assembly patterns under confinement still need to be addressed.

There are limitations in reaction efficiency under confinement, within self-assembled phases, or in solid-state systems.[20-22] Unlike solution-phase systems, reactions under confinement or in the solid state occur in highly restricted physicochemical environments, where molecular mobility and mass transport are significantly limited.[23-26] Such spatial confinement can unlock exceptional potential for enhancing reaction activity, controlling pathways, and improving product selectivity.[27-30] The organization of molecules (such as in crystalline state), interfacial migration, and restricted diffusion—along with steric confinement, solvation exclusion, and orientational effects—can significantly regulate reaction mechanisms, suppress side reactions, and enhance regio- and stereoselectivity.[31-34] The fixed conformation of reactants in the solid/confined state

may facilitate precise control over reaction sites and modes, and may allow stabilization of otherwise transient intermediates or inaccessible phases in solution.[35-37] Despite these advantages, the scope of solid-state reactions remains limited, largely due to restricted molecular mobility, hindered diffusion, and challenges in establishing catalytic cycles.[38-40] Many reactions have been successfully implemented in confined or solid phases, including [2+2] and [4+2] photocycloadditions, click reactions, boronic ester formation, and imine condensations.[41,42] These transformations generally proceed under catalyst-free and mild conditions, without the need for harsh thermal or cryogenic environments. Nonetheless, it remains an open question as to how many of the diverse covalent transformations developed by synthetic chemists can be adapted to confined systems. This underscores a rich landscape of chemical questions and properties worthy of in-depth investigation.[43,44] The development of dynamic covalent reactions for constructing responsive materials presents major challenges, particularly in the exploration of efficient chemical reactions.

Expanding the scope of such reactions from traditional crystalline systems to soft-matter or mesoscopic assembled phases is essential for enabling functionalities and applications.[45] For instance, dynamic chemical reactions in assembled molecular states are also critical to achieving supramolecular chirality evolution and the design of intelligent chiral materials.[46] Supramolecular chirality offers tunable, reversible, and stimuli-responsive characteristics, which can evolve through several mechanisms: chiral induction, chirality transfer and amplification during cooperative assembly, chirality inversion or reconstruction under external stimuli, and kinetic regulation under non-equilibrium conditions.[47-49] This multilevel chirality evolution lays a structural foundation for the development of stimuli-responsive chiral materials, chiral devices, and asymmetric catalytic platforms.[50-53] Furthermore, supramolecular chirality mediated by covalent or topochemical reactions offers a promising framework for the dynamic construction of advanced functional systems with chiral responsiveness.[54-57]

In this work, we introduce disulfide bond cleavage and aromatic nucleophilic substitution (S_NAr) reaction.[58,59] A pyrene-conjugated cystine derivative self-assembles into helical structures,

which encounters a reductant TCEP undergoing disulfide bond cleavage into cysteine (Fig. 1). In situ reaction (SS to SH) is quantitative in the self-assembled state, arising evolution of molecular arrangement. The supramolecular chirality is inherited from the pristine templates and distinct from the as-synthesized SH. Such reaction-mediated sacrificial templating protocol represents a top-down process in contrast to that of bottom-up. Further verification of such effect was carried out in a complex two-component system. Introducing pentafluoropyridine (PFP) provides significant π-hole/π interactions to give coassemblies (SS/PFP), which undergo reduction into another form (SH/PFP). Interestingly, under gentle heating with weak base ($NaHCO_3$), S_NAr occurs to give SPFP. The conversion yield from SS/PFP to SPFP in the aggregate state is determined up to 67%, which leads to the profound changes in the self-assembly behaviors and chiroptical activities. In the multiple step process, the evolution of chirality also exhibits inheritance or templating effect. Furthermore, the current protocol complements noncovalent chemistry by facilitating the construction of chiroptical materials and nanoarchitectures that are otherwise challenging to achieve.

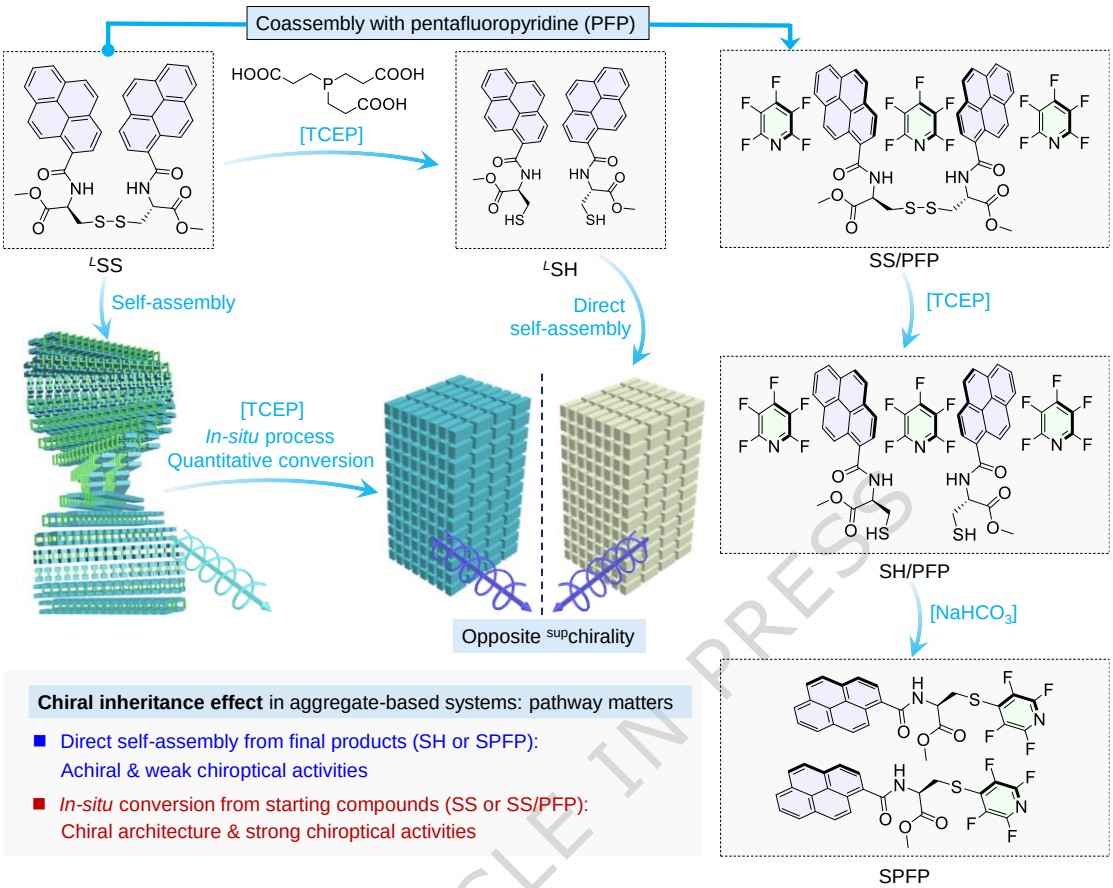

Figure 1. Topochemical conversion with inherited chiroptical properties. Molecular structures and topochemical conversion between different states. This special system shows the strong templating and inheritance with respect to the chiroptical performances.

Results

Disulfide bond is dynamic and redox sensitive. Its cleavage can be readily realized by reductant. SS with a cystine skeleton in the presence of a reductant TCEP transforms into SH (Fig. 2a, Supplementary Figs. 1-11). In dimethyl sulfoxide (DMSO), the disulfide bond cleavage was monitored by ^{1}H nuclear magnetic resonance (NMR) and high-resolution mass spectrometry (HRMS), which verified near quantitative conversion at ambient conditions (Fig. 2b). Fourier transform infrared (FTIR) spectroscopy confirms the emergence of S-H stretching vibration bands after reaction (Fig. 2c, Supplementary Fig. 12). The reaction leads to conformational variations. In DMSO with a high polarity, an excimer band at around 490 nm is retained (Fig. 2d), illustrating

the π-π stacking between pyrenes that SS adopts a folded geometry. Introducing TCEP witnesses the gradual disappearence of excimer emission, causing a luminescence color evolution from cyan to blue. The disulfide bond cleavage is dynamic and reversible.[60,61] Spontaneously, incubation at ambient condition shall recover the cyan luminescence, and the redox process is reversible for several cycles (Fig. 2e). We also evaluated the circular dichroism (CD) response (Fig. 2f, Supplementary Fig. 13, 14). SS possesses a bisignate Cotton effect centered at around 350 nm caused by the folded pyrenes, while SH affords an intrinsic Cotton effect with decreased intensity due to the absence of aromatic interplay in solution. Then, we explored the disulfide cleavage interaction conducted in the self-assembled state (in bulk water with less DMSO). During the initial self-assembly process, the assembly of SH and SS undergoes liquid–liquid phase separation (LLPS), which serves as a critical intermediate stage before the eventual formation of stable nanostructures, as directly visualized by SEM and TEM (Supplementary Figs. 15–26, 28–39). This LLPS transition profoundly influences the chiral evolution of the assemblies. In particular, our in situ chiroptical measurements (CD and UV–Vis spectra, Supplementary Figs. 27 and 40) revealed that the CD signals, especially the Cotton effect around 350 nm, underwent dramatic changes, including complete inversion, during the LLPS process before eventually stabilizing. Within the confined and dynamic environment of the LLPS droplets, molecular packing modes, interaction barriers, and nucleation pathways are altered. This allows the emergence of chiral conformations that can compete with or even override the initial chiral information. The eventual CD equilibrium corresponds to the thermodynamically or kinetically favored chirality after this complex maturation and selection process mediated by LLPS. Thus, the evolution of CD signals through the LLPS stage provides direct spectroscopic evidence that phase separation dynamically perturbs, and can ultimately redefine, the chiral outcome of the assembly.[62] Hydrophobic force drives the aggregation of SS, which encounters TCEP shall rapidly transform into SH in an in situ manner. The reaction in the self-assembled state is still efficient and can be completed within 15 mins (more TCEP is however required). High-performance liquid chromatography (HPLC) analysis on the collected self-assemblies treated by TCEP indicates a near quantitative conversion efficiency (Fig.

2g). This reaction could overcome the barrier of aggregates and achieves the in-situ transformation, favoring the topochemical process. It also realizes a profound blue-shift emission from 500 nm to 400 nm (Fig. 2h). SH no doubt adopts a distinct aromatic stacking that disfavors the excimer emission (such as CH-π), whereby the reaction degree could be well illustrated by the maxima emission wavelength. Individual SS and SH (as-synthesized) in the assembled state exhibit distinct Cotton effect (Fig. 2i). The dichroism intensity is enhanced compared to the monomer state in Fig. 1f, and both SS and SH give rise to overall bisignate type signal due to interplay between hydrophobic pyrenes. When conducted by in-situ protocol, $SH^{in\text{-}situ}$ display totally different shaped CD signal with SH or SS (Fig. 2j). It implies the topochemical transformation could retain the chiral properties of pristine structures with specific variations. We also evaluated the CPL properties of SS, SH and $SH^{in\text{-}situ}$ in the self-assembled state (Fig. 2k, 2l, Supplementary Fig. 41). Remarkably, SS and SH give opposite-handed CPL signal ascribed to the different stacking of pyrenes. However, the $SH^{in\text{-}situ}$ samples transformed directly from SS aggregates display same handedness with SS. It reflects a strong chiral inheritance effect. Topochemical conversion is not a bottom-up self-assembly process, but can be classified as a top-down process with a sacrificial templating feature. Based on the pathway-dependent chiroptical properties of SH assembly, we developed a fluorescence-based encryption strategy. Initially, the SS assembly exhibits green fluorescence originating from pyrene excimers, while the SH assembly emits blue monomer fluorescence, which allows the pre-encrypted message to be read visually. Encryption is initiated by adding TCEP to the SS assembly, which cleaves the disulfide bonds and shifts the fluorescence from green to blue, thereby erasing the original information. Although the encrypted SS assembly (after TCEP treatment) and the original SH assembly both show similar blue fluorescence under UV light, they possess distinct chiroptical signals due to their different assembly pathways. Decryption is accomplished through chiroptical spectroscopy (CD or CPL), where the unique Cotton effects associated with each assembly pathway allow the hidden pattern to be recovered. Under visible light, all samples appear identical, providing an additional layer of security. This pathway-encoded strategy prevents decryption based solely on the final chemical state,

demonstrating considerable potential for anti-counterfeiting applications. The SS pristine aggregate provides a chiral template or environment to refine the Cotton effect, CPL and other properties like nanomorphology.

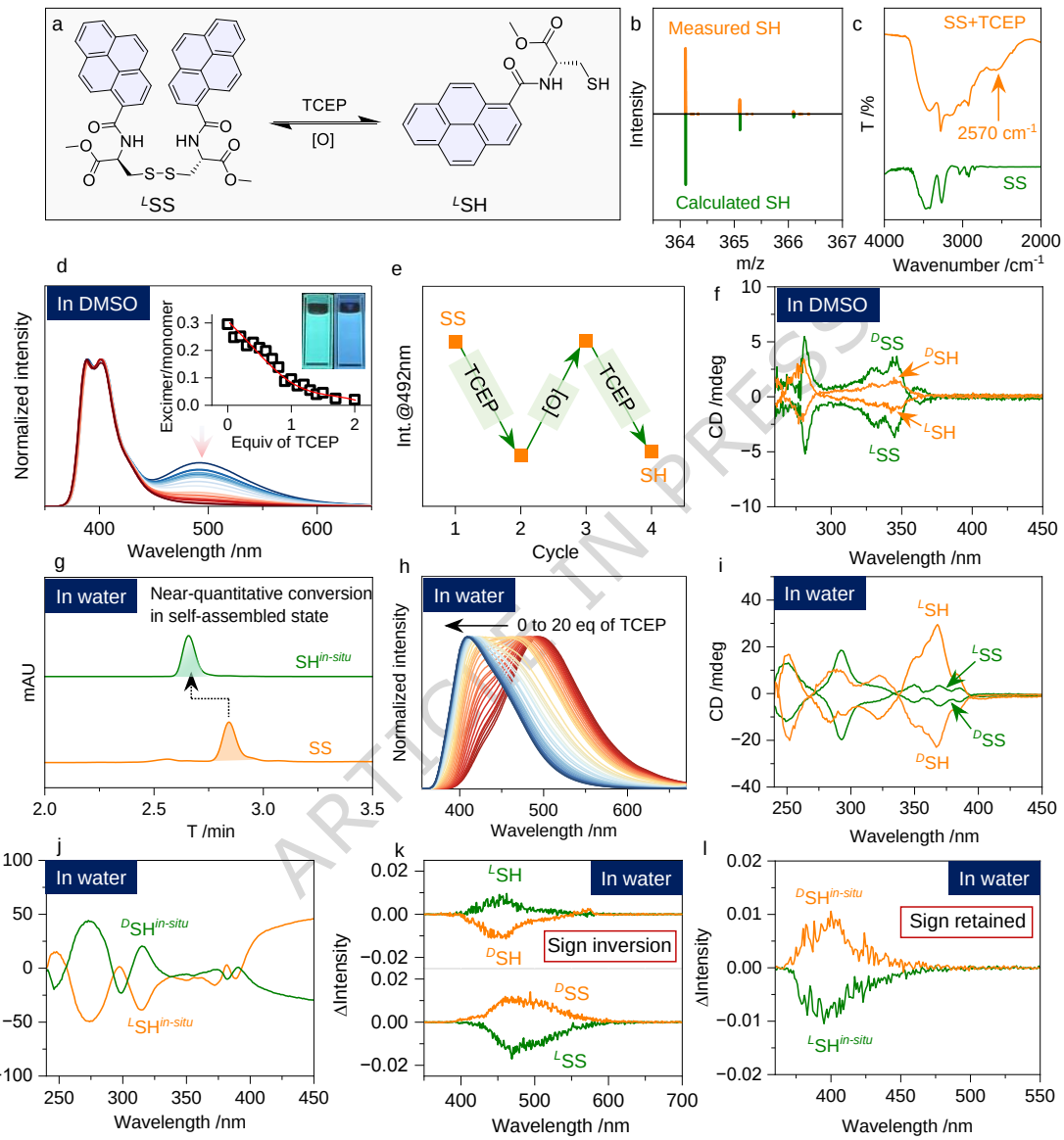

Figure 2. Redox-regulated dynamic chiroptical switch based on self-assembly. a) Conversion between SS and SH initiated by redox. b) HRMS spectrum comparison of SH. c) FTIR spectra of SS and after the addition of TCEP. d) Fluorescence spectra of SS in DMSO (0.1 mM) in the presence of different molar equiv. of TCEP (λ_{ex} = 340 nm). Insets show the decreasing trend of excimer relative intensities and bulky luminescence color change. e) Excimer emission intensity change cycles initiated by TCEP (2 equiv.) and spontaneous oxidization by air. f) CD spectra

comparison of SS and SH in DMSO (0.1 mM). g) HPLC tracking of SS and SH from in-situ conversion in the self-assembled state. h) Emission changes of SS in the self-assembled state with increasing amount of TCEP. i) CD spectra comparison between SS and SH (pre-synthesized) in the self-assembled state. j) CD spectra of SH in-situ converted from SS by adding TCEP. k) CPL spectra of SS and SH (pre-synthesized) in the self-assembled state (λ_{ex} = 340 nm). l) CPL spectra of SH in-situ converted from SS by adding TCEP (λ_{ex} = 340 nm). All self-assemblies were conducted in DMSO/H_2O (1/9, v/v) with a 0.4 mM concentration.

Next, we explored the evolution of nanoarchitectures and their molecular packing using scanning electron microscopy (SEM) and grazing incidence wide angle X-ray scattering (GIWAXS). SS individually self-assembled into fibrous structures (Fig. 3a, Supplementary Figs. 43-46), most of which adopt a twisted topology. ^{L}SS and ^{D}SS respectively give homochiral right-handedness (P) and left-handedness (M). It implies the high-fidelity chirality transfer from molecular to macroscopic scale. The expression of chirality at macroscopic level is facilitated by the one-dimensional packing, and folded pyrene with relatively rigid skeleton favors the packing into helical sense. In comparison, SH (pre-synthesized) tends to crystallize into microrods. The three-dimensional growth hinders the chiral expression at macroscopic scale. The missing of disulfide bond leads to the unfolding without intramolecular constraints that improves the ordered packing. In contrast, we synthesized the self-assemblies from $SH^{in\text{-}situ}$ by directly adding TCEP to the SS aggregates. In the similar way, it observed the emergence of microrods with highly crystalline domains. However, the architectures are relatively larger than that of SH alone, which might be originated from the slow molecular exchange between reagents and products with more thermodynamic control pathways. It should be noted, even those SH and $SH^{in\text{-}situ}$ did not show macroscopic chirality probed by SEM, their chiroptical responses verified the presence of supramolecular chirality, which are accounted to the local or overall asymmetric packing of building units. Given the significant (approximately 200-fold) increase in particle width upon reduction, it is likely that the assemblies underwent partial or complete structural reorganization

into a new form in the SH state. Nevertheless, the distinct chiroptical spectral differences strongly suggest that the original SS assemblies acted as seeds or templates during reduction, thereby guiding the asymmetric stacking orientation of the newly formed SH assemblies. This observation demonstrates an effective chiral transfer or chiral memory effect. GIWAXS provides detailed and anisotropic molecular packing information, where Q_{xy} and Q_z record the lattice parameters perpendicular and parallel to the one-dimensional growth direction (inset of Fig. 3b). Based on the 2D scattering pattern and the corresponding integral profiles, Q_z and Q_{xy} bands are basically locate below and higher than 1.0 $Å^{-1}$. For SS, the several pronounced peaks at Q_z direction are assigned as the lattice parameters, and the primary d-spacing of 13.4 Å can be designated as the interlayer distance (molecular length of a SS). 3.8 and 3.17 Å correspond to the π-π stacking of pyrenes. SH apparently adopts a distinct packing modality. The 1st and 2nd d-spacings at 8.72 and 6.54 Å show that it is in an interdigitated array with shrunk packing parameters. The Q_{xy} plane with three major bands of 3.56, 3.23 and 2.90 Å is contributed by the π-π and CH-π short contacts between pyrenes. $SH^{in\text{-}situ}$ has scattering patterns different with both SH and SS. There are larger d-spacings found at Q_z direction including 12.3 and 10.3 Å, confirming the templating effects of SS. A sharp band at 3.47 Å is accounted to the packing of pyrenes. The results are in good agreement with the chiral inheritance found in CD and CPL activities.

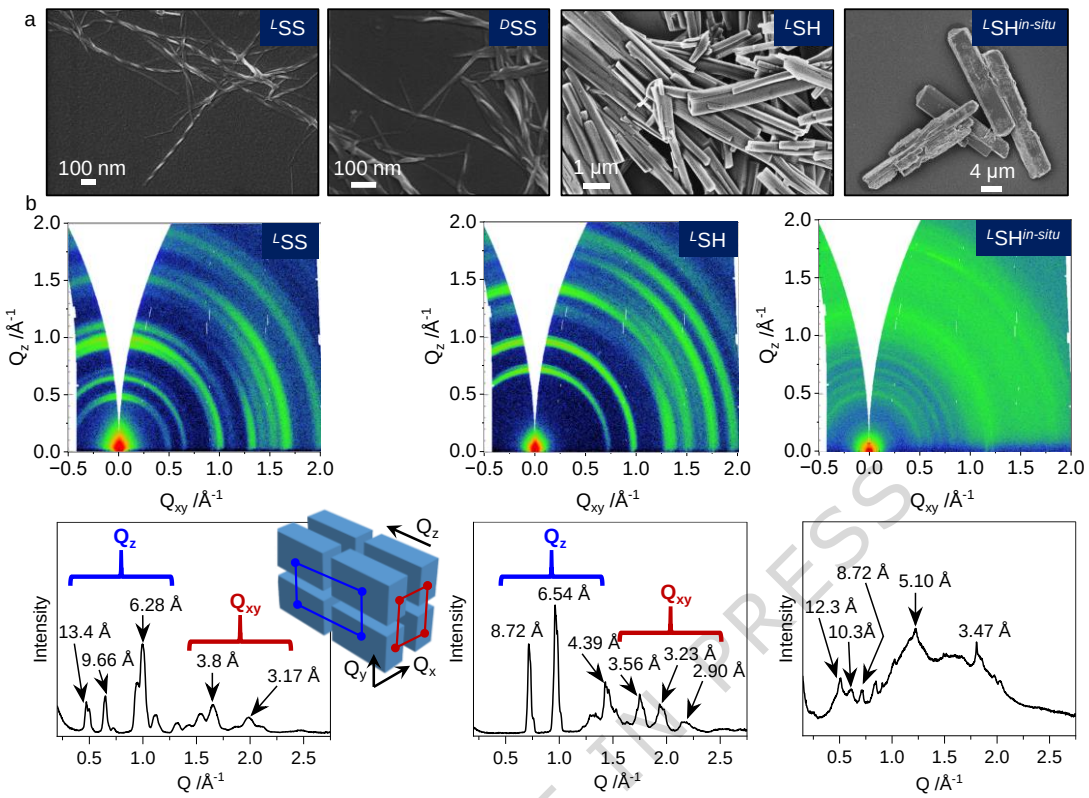

Figure 3. Morphological and structural characterization of self-assemblies. a) SEM images of different self-assemblies. b) The GIWAXS patterns and integral curves. All self-assemblies were conducted in DMSO/H_2O (1/9, v/v) with a 0.4 mM concentration.

The above discussions illustrate the disulfide bond cleavage into SH with great changes in nanoarchitectures with chiral inheritance. Due to the presence of folded pyrene moieties, SS might be capable of clamping or coassemble with electron-deficient compounds through π-hole/π interactions.[63,64] Thereafter, we could realize disulfide bond cleavage in a two-component system (Fig. 4a). PFP with a perfluorinated aromatic core was introduced. In self-assembled state, the gradual addition of excess PFP witnesses the enhanced monomeric emission of SS (Fig. 4b, excess PFP was added in order to overcome its solvation effect). It implies that PFP inserts into the aromatic packing arrays to afford coassembled arrangements. Decreasing tendency was found in CD spectra upon adding PFP (Fig. 4c, Supplementary Fig. 47). Between 325 nm to 400 nm, the pristine intrinsic Cotton effects becomes bisignate ascribed to the aromatic complexation between

pyrenes and PFPs. SEM images on the two-component coassemblies show the similar twisted fibers with identical handedness that ^{L}SS/PFP and ^{D}SS/PFP give rise to P- and M-handedness (Fig. 4d, Supplementary Figs. 48, 49). We did not observe the presence of phase separation or self-sorting of individual aggregation. It is believed that partial insertion of PFP into the coassembly array of SS which act as a chiral matrix is plausibly a dominating pathway. Using different equiv. of TCEP to control the cleavage degree of disulfide bond, SS/PFP gradually converted to SH/PFP, with decreasing excimer emission and enhanced monomeric emission at around 400 nm (Fig. 4e). The normalized emission spectra display difference with the SS sample without PFP (Fig. 2h). SS/PFP exhibits strong and persistent band at around 400 nm because PFP could bind to pyrenes either in the SS or SH form. CD spectra, however, were hardly altered after disulfide bond cleavage. It further confirms the presence of templating and chiral inheritance effect during the topochemical process (Fig. 4f, Supplementary Fig. 50). SS/PFP and SH/PFP are both CPL active (Fig. 4g, 4h, Supplementary Fig. 51), and both exhibit *l*- and *r*-CPL in the D- and L-enantiomeric form with however different maxima wavelengths at 500 and 400 nm respectively. The in-situ generated coassemblies of SH/PFP$^{\text{in-situ}}$ show similar feature to SH/PFP due to the complete conversion from SS to SH in the aggregated state. SEM probed the morphologies of PFP coassemblies (Fig. 4i, Supplementary Figs. 52-54). Incorporating PFP into SH (as-synthesized) assembly witnesses the presence of nanorods with lateral width and length rather smaller than SH alone. Clearly, coassembly with a second component decreases the three-dimensional tendency by directional π-hole/π forces. In-situ fabrication of SH/PFP coassembly produced relatively larger constructs. This behavior is quite similar to the system without PFP.

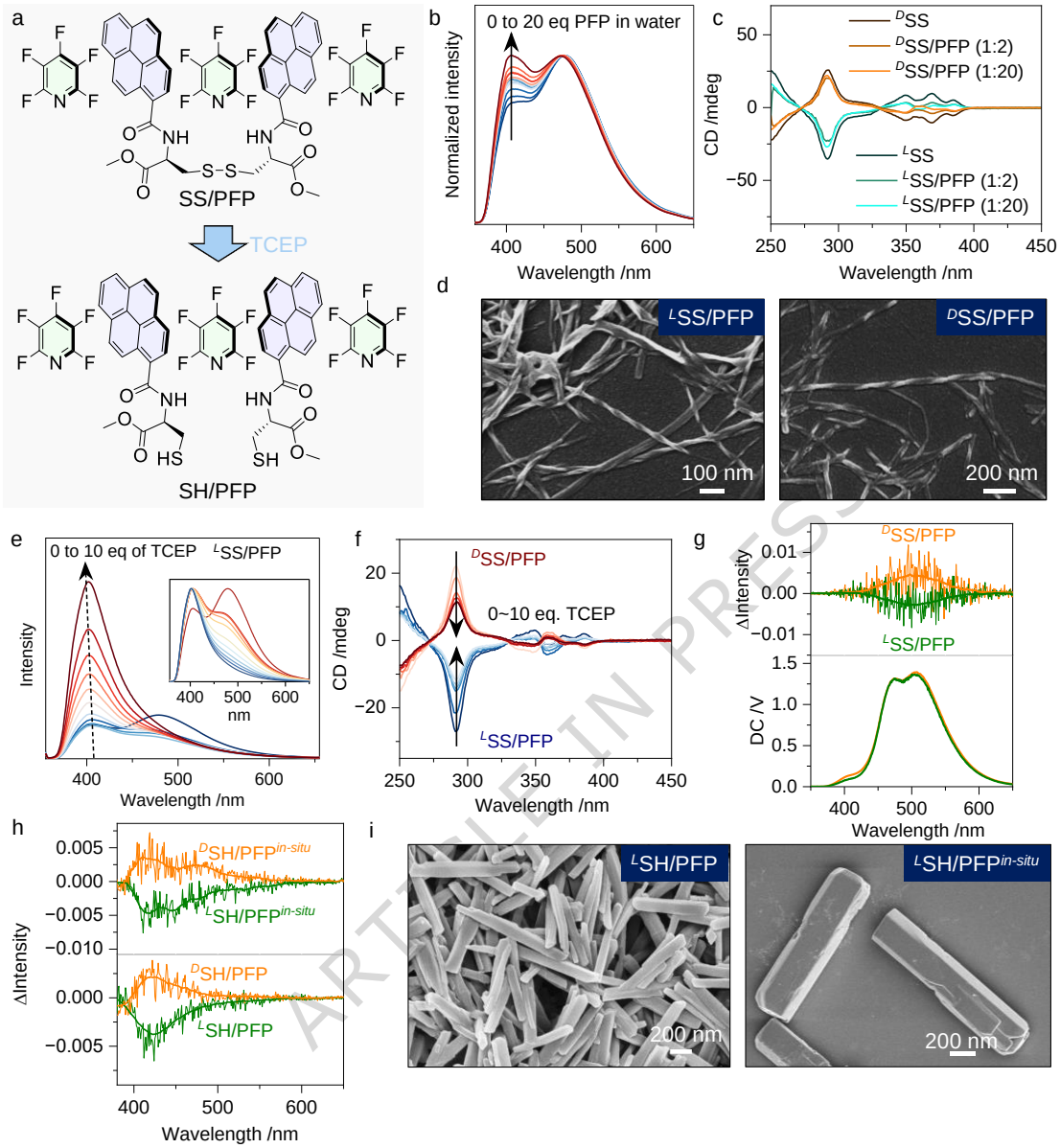

Figure 4. Redox-modulated chiroptical switching in co-assemblies. a) Conversion from SS/PFP to SH/PFP via TCEP-mediated disulfide bond cleavage. b,c) Emission and CD spectrum changes of SS with the addition of PFP. d) SEM images of coassembled SS/PFP. e,f) Emission and CD spectrum changes under different reduction state. Inset shows the normalized spectra. g,h) CPL spectra of SS/PFP and SH/PFP coassemblies. i) SEM images of ^{L}SH/PFP and ^{L}SH/PFP$^{in\text{-}situ}$. All self-assemblies were conducted in DMSO/H_2O (1/9, v/v) with a 0.4 mM concentration.

SH/PFP coassembly system is potentially reactive. The para-position F could readily be

substituted by sulfhydryl group catalyzed by base. After optimization, the reaction could be initiated in solution (DMSO) in the presence of gentle heating and a weak base $NaHCO_3$ (Fig. 5a). The product of SPFP was obtained and fully characterized by ^{1}H, ^{19}F NMR and HRMS (Fig. 5b). It allows for an alternative protocol to enable topochemical conversion. However, it still faces one big challenge that how efficient the S_NAr can be in the self-assembled state. A two-step in situ conversion was conducted. SS/PFP coassemblies were prepared, followed by the addition of TCEP. After incubation, $NaHCO_3$ powder was then added. The final mixture was incubated in a 60 ºC oven. Then the self-assemblies were collected by high-speed centrifuge, and subjected to HPLC analysis (Fig. 5c). It shows that the presence of SPFP after two in-situ steps, which gives a 67% yield. There is almost no side product with however remaining SH. It illustrates the pathway is feasible to give topochemically self-assembled products. One pronounced behavior is the changes of fluorescence. S-substituted PFP constitutes into a typical D-π-A conjugate with cyan emission. Therefore, the addition of $NaHCO_3$ to SH/PFP system enables the luminescent color evolution from blue to cyan (~490 nm, Fig. 5d). The CD spectra show different features with the SH/PFP (Fig. 5e, Supplementary Fig. 55), that strong exciton bands were observed between 400 to 250 nm, implying the electronic interplay between the aromatic planes. This reaction promotes us to further explore the templating effect between as-synthesized and in-situ converted SPFP. Probed by CPL (Fig. 5f, Supplementary Fig. 56), the two step in-situ sample show stronger CPL intensity as well as the dissymmetry g-factors (±0.005) than the as-synthesized SPFP (±0.002). It is plausibly stemmed from the chiral inheritance effect as SS has a preference self-assembling into helical structures with enhanced chiral expression. It is worth noting that, the CPL of in-situ converted SPFP is blue-shifted compared to that of as-synthesized samples, which is caused by the incomplete conversion as discussed in Fig. 4c. With respect to nanomorphology, SPFP alone affords an achiral long and thin fibers (Fig. 5g, Supplementary Figs. 57-59). SPFP alone failed to express chirality at macroscopic scale. The nanoarchitectures were greatly altered undergoing a topochemical process. Starting from SH/PFP, the $SPFP^{in\text{-}situ}$ gives ribbon-like geometry with enlarged size to microscale, which stems from the giant crystalline states of SH coassembly. In

contrast, SPFP$^{in\text{-}situ}$ underwent two-step topochemical process starting from SS/PFP is chiral. It illustrates the vital importance of templating and inheritance effect of starting materials, which also in consistent with the strong CPL g-factor compared to the as-synthesized SPFP.

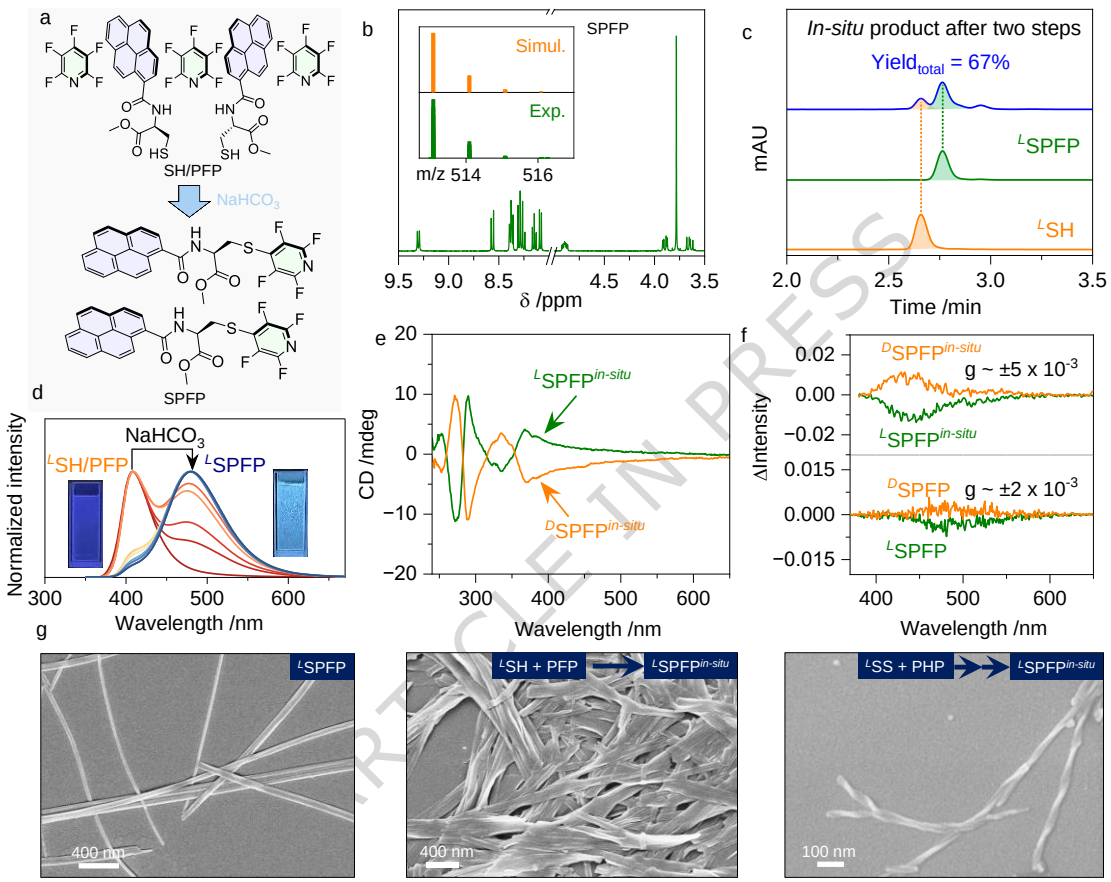

Figure 5. In-situ covalent transformation and chiroptical property evolution in self-assemblies. a) Conversion from SH/PFP to SPFP by base-catalyzed aromatic S$_N$Ar reaction. b) ^{1}H NMR (DMSO-d_6, 400 MHz) and HRMS spectra of SPFP obtained from the in-situ reaction. c) HPLC curves of the product after two in-situ reactions by disulfide bond cleavage and S$_N$Ar starting from the mixture of ^{L}SS and PFP. d) Emission changes from SH/PFP to SPFP controlled by the different amount of base in the self-assembled state (λ_{ex} = 340 nm). e) CD spectra of the in-situ generated SPFP from SH/PFP. f) CPL spectra comparison between as-synthesized and in-situ generated SPFP from SS/PFP. g) SEM images of as-synthesized and in-situ generated SPFP (from SH/PFP and SS/PFP). All self-assemblies were conducted in DMSO/H$_2$O (1/9, v/v) with a 0.4 mM

concentration. [PFP] = 8 mM, [$NaHCO_3$] = 0.8 mM.

Finally, we carried out molecular dynamics (MD) simulation to gain a deep understanding about the aggregation in different combinations (Supplementary Figs. 60-64). Five self-assembly systems including SS, SH, SS/PFP, SH/PFP and SPFP were conducted under same simulation conditions. The free monomers have propensity to form aggregates accompanied by the desolvation. Solvophobic force, hydrogen bonding and aromatic stacking are recognized as the major contributions to aggregation. We analyzed the dominant dimer structures extracted from ^{L}SS MD simulations. By fixing the pyrene rings and optimizing the amino acid residues, the ^{L}SH and ^{L}SPFP structural pathways were selected, enabling the assemblies to exhibit a chiral inheritance effect. The CD and absorption spectra of the corresponding structures, calculated using the B3LYP-D3/6-311(d) basis set, showed good agreement with experimental values (Supplementary Fig. 65). The snapshots after 10 ns equilibrium were representatively shown in Fig. 6a. Starting at 0 ns as the freely dispersion, SS and PFP spontaneously self-assemble into alternatively packed arrays, which are designated as the typical π-hole/π interaction. In SPFP state, they also adopt the π-hole/π stacking between substituted PFP and pyrene moieties. This interaction occurs both in the intramolecular and intermolecular manner, indicating a folding is possible. Electrostatic potentials (ESP) were calculated (Fig. 6b).[65] Pyrene as a typical π-electron sufficient segment features negative and positive ESP at interior and exterior regions due to the electron negativity of carbon and hydrogen. The maximum of interior is determined as -16 kcal/mol. The pyridine and perfluorination enable a strong π-hole region in PFP, where the maximum ESP was determined as high as 42.3 kcal/mol. Thus, pyrene and PFP are excellent pairs to allow π-hole/π complexation. We also collected the statistic parameters including the number of hydrogen bonds and short distance pairs within 0.35 nm (Fig. 6c). SS and SH coassembly systems possess similar number of hydrogen bonds, while SPFP gives more hydrogen bonds. With increasing equilibrium time, the number of hydrogen bonds increase sharply from near zero to about 100 (for 200 SS or 400 SH molecules). The π-hole/π and hydrogen bonding drive the aggregation of building units with

decreased solvent accessible surface areas (SASA). Transformation from SS to SH increases the hydrophilic SASA. This can be also observed in the coassembled SS/PFP system. Radial distribution function (RDF) profiles were statistically collected (Fig. 6d). Pyrene-pyrene distances (labeled atoms can be found in the SI) in SS were widely distributed from 0.38 to 0.61 nm, which might be caused by the folded pyrene dimers that constrain the ordered intermolecular π-π stacking. After disulfide bond cleavage, a sharp band at 0.38 nm was found, corresponding to the π-π stacking between SH. By introducing PFP, the possibility g(r) values were enhanced with a strong peak at 0.36 nm, indicative of the π-hole/π arrays between pyrene and PFPs, in good agreement with the MD snapshots in Fig. 6a.

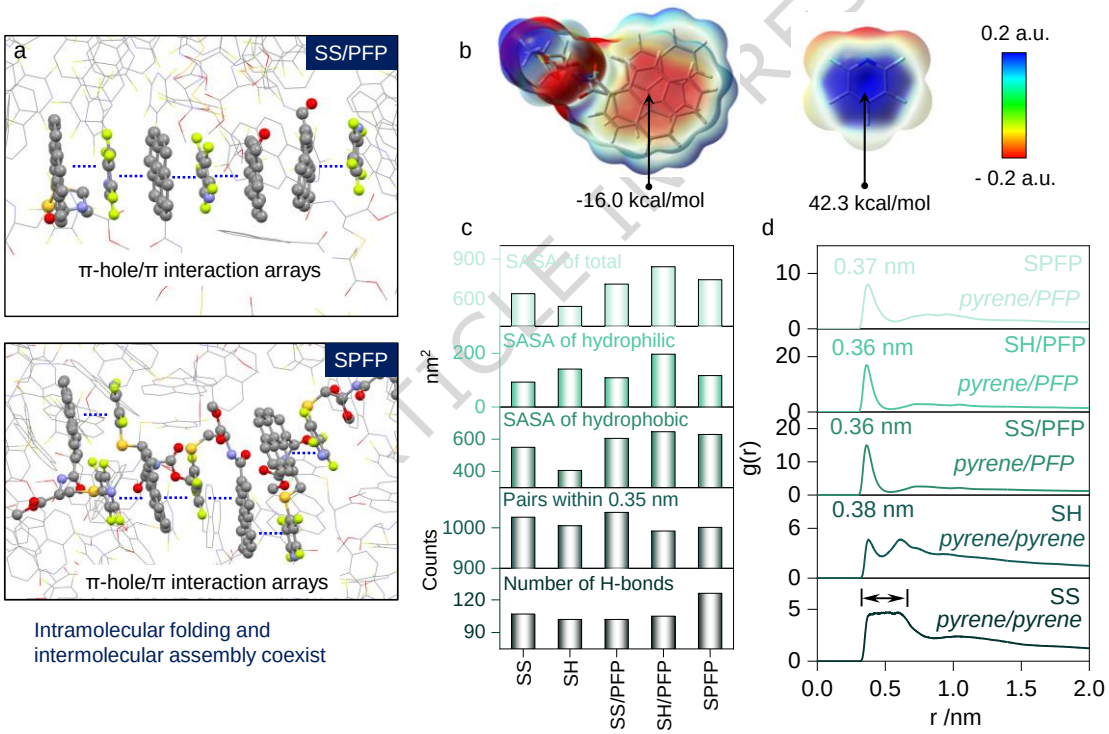

Figure 6. Molecular dynamics study of non-covalent interactions and assembly characteristics. a) Snapshot of SS/PFP and SPFP MD simulations, where show the π-hole/π interaction arrays. b) ESP maps and the maxima values of SS and PFP. c) Number of hydrogen bonds, pairs within 0.35 nm, and SASA files of different MD simulations. d) RDF curves between pyrenes and pyrene/PFP in different MD simulations.

Discussion

In summary, we report an aromatic cystine conjugate system that shows topochemical conversion undergoing reduction and S_NAr reactions. SS alone self-assembled into helical nanoarchitectures, which converted to crystalline rods after disulfide bond cleavage triggered by TCEP. Compared to the as-synthesized SH under a bottom-up self-assembly, the in-situ converted SH inherited the chiral information from pristine aggregates of SS. The chiral inheritance and templating effect were further verified in the coassembled complexes with PFP. PFP provides π-hole/π interaction to constitute with SS into coassemblies, which went through reduction and S_NAr reaction to afford SPFP with high yields (67%) in the confined aggregated state. The in-situ transformed PFP shows distinct properties with the as-synthesized building unit. And due to the chiral inheritance and templating effect from chiral, asymmetric g-factors of CPL was enhanced with retained chiral nanoarchitectures.

Methods

Materials

All commercial chemicals were used as received. The synthesis procedures are described in Supplementary Fig. 1-11.

Self-assembly protocol

Self-assembly was initiated via a solvent exchange protocol. The compounds were pre-dissolved in dimethyl sulfoxide (DMSO) stock solutions (4 mM) after ultrasonic dissolution. By injecting certain volume stock solution (200 μL for instance) into bulky deionized water (1800 μL for instance), followed by aging at ambient conditions for 8 h before testing, a self-assembly system was achieved (0.4 mM). The volume ratio of DMSO and water was fixed at 1:9. To prepare the co-assemblies, the compounds were pre-dissolved in DMSO stock solution (8 mM) after ultrasonic dissolution. Compound SS solution (100 μL) and pentafluoropyridine solution (100 μL) were transferred to a test tube, and then 1800 μL of water was added to prepare a co-assembly solution

(0.4 mM). Two-step in situ transformation. SS and PFP compounds were dissolved in DMSO to obtain a stock solution, 100 μL of each was mixed, then deionized water (1800 μL) was added for mixing, and the reducing agent TCEP was added to equilibrate the mixture for a period of time at room temperature, then sodium bicarbonate ($NaHCO_3$) was added, and the reaction mixture continued to be reacted at a constant temperature at 60 °C in an oven. After 5 days of incubation, the reaction solution was transferred to a centrifuge tube and centrifuged to remove the solvent to obtain the of the reaction. Other samples of different concentrations were kept at a DMSO and water volume ratio of 1:9. Unspecified, all samples tested were used in the *L* configuration.

Measurement of NMR and High-resolution mass spectra.

^{1}H NMR, ^{19}F NMR and ^{13}C NMR spectra were recorded on a Bruker ADVANCE III 400 spectrometer in DMSO-d_6 at 298 K. High-resolution mass spectra (HR-MS) were performed on an Agilent Q-TOF 6510.

Scanning electron microscope characterizations

SEM images were acquired using a Zeiss scanning electron microscope (Germany). For imaging, the samples were deposited onto a single-crystal silicon wafer, dried, and then sputter-coated with a thin layer of gold to enhance conductivity and contrast prior to measurement.

Fourier transform infrared spectra

FT-IR spectra were recorded on Tensor II FT-IR spectrometer. Prior to measurement, all samples were thoroughly dried, homogenized with KBr, and pressed into pellets for analysis.

UV-Visible absorption spectra

UV-Visible absorption spectra were recorded at room temperature using a Shimadzu UV-1900 spectrophotometer. Absorption measurements were performed in a quartz cuvette.

Fluorescence spectra

The fluorescence spectra were recorded on a RF 6000 Shimadzu fluorophotometer.

Circular dichroism spectra and Circularly polarized luminescence spectra

Circular dichroism (CD) and circularly polarized luminescence (CPL) were measured with an Applied Photophysics ChirascanV100 model. Chiroptical testing is performed using quartz glass.

Density functional theory (DFT) computation and molecular dynamics (MD) simulations.

Initial configurations of the acceptor molecule and the pyrene-modified amino acid were constructed from Chem3D structures. These calculations employed Density Functional Theory (DFT) at the B3LYP-D3/ 6-311G (d,p) level of theory. Topology files were generated using Amber, ACPYPE, and Gaussian tools, ensuring compatibility with the GROMACS force field. We inserted 400 molecules (200 cystine molecules) randomly into the box (10 nm × 10 nm × 10 nm), followed by solvation with the SPC216 water model. Simulations were performed using GROMACS at 298 K for 10 ns with a time step of 2 fs. Cartesian coordinates of the optimized structures are provided in the Source Data.

Data Availability

All relevant data generated or analyzed during this study can be obtained from the corresponding author. The Supplementary Information is available in the online version of the paper. Source data are provided with this manuscript.

References

1. Yashima, E.; Ousaka, N.; Taura, D.; Shimomura, K.; Ikai, T.; Maeda, K. Supramolecular Helical Systems: Helical Assemblies of Small Molecules, Foldamers, and Polymers with Chiral Amplification and Their Functions. *Chem. Rev.* **2016**, 116, 13752– 13990.
2. Jia, X.; Zhu, L. Photoexcitation-Induced Assembly: A Bottom-Up Physical Strategy for

Driving Molecular Motion and Phase Evolution. *Acc. Chem. Res.* **2023**, 56, 655– 666.

3. Kumar, J.; Nakashima, T.; Kawai, T. Circularly Polarized Luminescence in Chiral Molecules and Supramolecular Assemblies. *J. Phys. Chem. Lett.* **2015**, 6, 3445– 3452.
4. Behera, P.; May, M. A.; Gómez-Ortiz, F.; Susarla, S.; Das, S.; Nelson, C. T.; Caretta, L.; Hsu, S.-L.; McCarter, M. R.; Savitzky, B. H.; Barnard, E. S.; Raja, A.; Hong, Z.; García-Fernandez, P.; Lovesey, S. W.; van der Laan, G.; Ercius, P.; Ophus, C.; Martin, L. W.; Junquera, J.; Raschke, M. B.; Ramesh, R. Electric Field Control of Chirality. *Sci. Adv.* **2022**, 8, eabj8030.
5. Li, J.; Cui, Y.; Lu, Y.-L.; Zhang, Y.; Zhang, K.; Gu, C.; Wang, K.; Liang, Y.; Liu, C.-S. Programmable Supramolecular Chirality in Non-equilibrium Systems Affording a Multistate Chiroptical Switch. *Nat. Commun.* **2023**, 14, 5030.
6. Xing, P.; Zhao, Y. Controlling Supramolecular Chirality in Multicomponent Self-Assembled Systems. *Acc. Chem. Res.* **2018**, 51, 2324– 2334.
7. Ren, X.; Zou, Q.; Yuan, C.; Chang, R.; Xing, R.; Yan, X. The Dominant Role of Oxygen in Modulating the Chemical Evolution Pathways of Tyrosine in Peptides: Dityrosine or Melanin. *Angew. Chem., Int. Ed.* **2019**, 58, 5872– 5876.
8. Wang, Y.; Rencus-Lazar, S.; Zhou, H.; Yin, Y.; Jiang, X.; Cai, K.; Gazit, E.; Ji, W. Bioinspired Amino Acid Based Materials in Bionanotechnology: From Minimalistic Building Blocks and Assembly Mechanism to Applications. *ACS Nano.* **2024**, 18, 1257– 1288.
9. Yuan, W.; Chen, L.; Yuan, C.; Zhang, Z.; Chen, X.; Zhang, X.; Guo, J.; Qian, C.; Zhao, Z.; Zhao, Y. Cooperative Supramolecular Polymerization of Styrylpyrenes for Color-Dependent Circularly Polarized Luminescence and Photocycloaddition. *Nat. Commun.* **2023**, 14, 8022.
10. Wu, A. L.; Guo, Y. X.; Li, M. Q.; Li, Q.; Zang, H. C.; Li, J. B. Tunable chirality of self-assembled dipeptides mediated by bipyridine derivative. *Angew. Chem., Int. Ed.* **2023**, 62, e202314368.
11. Zhao, C.; Wang, Y.; Jiang, Y.; Wu, N.; Wang, H.; Li, T.; Ouyang, G.; Liu, M. Handedness-Inverted and Stimuli-Responsive Circularly Polarized Luminescent Nano/Micromaterials Through Pathway-Dependent Chiral Supramolecular Polymorphism. *Adv. Mater.* **2024**, 36,

2403329.

12. Li, J. J.; Yin, F.; Wang, J. H.; Du, H. C.; Xu, F.; Meskers, S.; Li, Y. D.; Wijker, S.; Peng, Y.; Bellan, R.; Vantomme, G.; Song, J.; Liu, C.-S.; Meijer, E. W. Self-Regulating Hydrogel with Reversible Optical Activity in Its Gel-to-Gel Transformation. *J. Am. Chem. Soc.* **2025**, 147, 17361– 17371.
13. Chang, R.; Yuan, C.; Zhou, P.; Xing, R.; Yan, X. Peptide Self-Assembly: From Ordered to Disordered. *Acc. Chem. Res.* **2024**, 57, 289– 301.
14. Zhang, H.; Han, J.; Jin, X.; Duan, P. Improving the Overall Properties of Circularly Polarized Luminescent Materials Through Arene-Perfluoroarene Interactions. *Angew. Chem. Int. Ed.* **2021**, 60, 4575– 4580.
15. Grossmann, L.; King, B. T.; Reichlmaier, S.; Hartmann, N.; Rosen, J.; Heckl, W. M.; Bjork, J.; Lackinger, M. On-surface Photopolymerization of Two-dimensional Polymers Ordered on the Mesoscale. *Nat. Chem.* **2021**, 13, 730– 736.
16. Zhong, H.; Zhao, B.; Deng, J. Solvent-Dependent Chirality Transmission and Amplification from Cellulose Derivative to Achiral Helical Polymer for Achieving Full-Color and White Circularly Polarized Luminescence. *Angew. Chem., Int. Ed.* **2025**, 64, e202418463.
17. Zhang, S.; Chen, A.; An, Y.; Li, Q. Arene-perfluoroarene Interaction: Properties, Constructions, and Applications in Materials Science. *Matter.* **2024**, 7, 3317– 3350.
18. Peluso, P.; Chankvetadze, B. Recognition in the Domain of Molecular Chirality: From Noncovalent Interactions to Separation of Enantiomers. *Chem. Rev.* **2022**, 122, 13235– 13400.
19. Gao, J., Ouyang, G., Zhou, P., Shang, P., Long, H., Ji, L., Qu, Z., Guo, M., Yang, Y., Zhao, F., Yin, X., Ke, Y., Wei, Z., Zhang, Z., Yan, X., Liu, M., Qiao, Y. & Song, Y. Spatiotemporal-dependent Confinement Effect of Bubble Swarms Enables a Fractal Hierarchical Assembly with Promoted Chirality. *J. Am. Chem. Soc.* **2024**, 146, 18104–18116.
20. Wang, Z.; Xie, X.; Hao, A.; Xing, P. Multiple-State Control over Supramolecular Chirality through Dynamic Chemistry Mediated Molecular Engineering. *Angew. Chem., Int. Ed.* **2024**, 63, e202407182.

21. Sahoo, J. K.; Pappas, C. G.; Sasselli, I. R.; Abul-Haija, Y. M.; Ulijn, R. V. Biocatalytic Self-Assembly Cascades. *Angew. Chem., Int. Ed.* **2017**, 56, 6828– 6832.
22. Hao, W.; Li, Y.; Liu, M. Endowing Phosphor Materials with Long-Afterglow Circularly Polarized Phosphorescence via Ball Milling. *Adv. Optical Mater.* **2021**, 9, 2100452.
23. Wang, Z.; Chu, C.; Hao, A.; Xing, P. Dynamic Borate Esterification for Evolved Supramolecular Chirality and Chiral Optics. *Angew. Chem., Int. Ed.* **2025**, 64, e202504617.
24. Liu, Y.; Guan, X.-R.; Wang, D.-C.; Stoddart, J. F.; Guo, Q.-H. Soluble and Processable Single-Crystalline Cationic Polymers. *J. Am. Chem. Soc.* **2023**, 145, 13223– 13231.
25. Hu, F.; Hao, W.; Mücke, D.; Pan, Q.; Li, Z.; Qi, H.; Zhao, Y. Highly Efficient Preparation of Single-Layer Two-Dimensional Polymer Obtained from Single-Crystal to Single-Crystal Synthesis. *J. Am. Chem. Soc.* **2021**, 143, 5636– 5642.
26. Cao, M.; Cao, C.; Zhou, P.; Wang, N.; Wang, D.; Wang, J.; Xia, D.; & Xu, H. Self-assembly of Amphiphilic Peptides: Effects of the Single-chain-to-gemini Structural Transition and the Side Chain Groups. *Colloids Surf. A.* **2015**, 6, 7419.
27. Wang, H.; Wang, Y.; Shen, B.; Liu, X.; Lee, M. Substrate-Driven Transient Self-Assembly and Spontaneous Disassembly Directed by Chemical Reaction with Product Release. *J. Am. Chem. Soc.* **2019**, 141, 4182– 4185.
28. Zhang, Q.; Crespi, S.; Toyoda, R.; Costil, R.; Browne, W.; Qu, D.; Tian, H.; Feringa, B. Stereodivergent Chirality Transfer by Noncovalent Control of Disulfide Bonds. *J. Am. Chem. Soc.* **2022**, 144, 4376– 4382.
29. Morimoto, M.; Bierschenk, S. M.; Xia, K. T.; Bergman, R. G.; Raymond, K. N.; Toste, F. D. Advances in Supramolecular Host-mediated Reactivity. *Nat. Catal.* **2020**, 3, 969– 984.
30. Raymond, D. M.; Nilsson, B. L. Multicomponent Peptide Assemblies. *Chem. Soc. Rev.* **2018**, 47, 3659– 3720.
31. Hema, K.; Ravi, A.; Raju, C.; Sureshan, K. M. Polymers with Advanced Structural and Supramolecular Features Synthesized through Topochemical Polymerization. *Chem. Sci.* **2021**, 12, 5361– 5380.

32. Yang, C.; Liu, J.; Khoo, R.; Abdelsamie, M.; Qi, M.; Li, H.; Mao, H.; Hemenway, S.; Xu, Q.; Wang, Y.; Yu, B.; Zhang, Q.; Liu, X.; Klivansky, L.; Gu, X.; Zhu, C.; Reimer, J.; Cui, G.; Sutter-Fella, C.; Zhang, J.; Ren, G.; Liu, Y. High-fidelity Topochemical Polymerization in Single Crystals, Polycrystals, and Solution Aggregates. *Nat. Commun.* **2025**, 16, 3498.
33. Wang, Z.; Gai, Y.; Hao, A.; Xing, P. Superhelical Self-Assembly of Microcrystals from Cyclodipeptides. *Angew. Chem., Int. Ed.* **2025**, 64, e202501832.
34. Sarojini, V.; Glossop, H. Accessing the Thiol Toolbox: Synthesis and Structure–Activity Studies on Fluoro-Thiol Conjugated Antimicrobial Peptides. *Bioconjugate Chem.* **2023**, 34, 1, 218– 227.
35. Andrews, K. G.; Piskorz, T. K.; Horton, P. N.; Coles, S. J. Enzyme-like Acyl Transfer Catalysis in a Bifunctional Organic Cage. *J. Am. Chem. Soc.* **2024**, 146, 17887– 17897.
36. Hess, S.; Coppola, F.; Dang, V.; Tran, P.; Mickel, P.; Oktawiec, J.; Ren, Z.; Král, P.; Nguyen, A. Noncovalent Peptide Assembly Enables Crystalline, Permutable, and Reactive Thiol Frameworks. *J. Am. Chem. Soc.* **2023**, 145, 19588– 19600.
37. Qiu, X.; Chen, L.; Hou, J.; Lin, H.; Xu, T.; Tong, F.; Tian, H.; Qu, D. Regulating Reversible Untwisting and Twisting Motions in Helical Dynamic Molecular Crystals. *J. Am. Chem. Soc.* **2025**, 147, 17772–17783.
38. Panja, S.; Adams, D. J. Stimuli-Responsive Dynamic Transformations in Supramolecular Gels. *Chem. Soc. Rev.* **2021**, 50, 5165– 5200.
39. Ji, W.; Yuan, C.; Chakraborty, P.; Makam, P.; Bera, S.; Rencus-Lazar, S.; Li, J.; Yan, X.; Gazit, E. Coassembly-Induced Transformation of Dipeptide Amyloid-Like Structures into Stimuli-Responsive Supramolecular Materials. *ACS Nano.* **2020**, 14, 7181– 7190.
40. Dou, X.; Mehwish, N.; Zhao, C.; Liu, J.; Xing, C.; Feng, C. Supramolecular Hydrogels with Tunable Chirality for Promising Biomedical Applications. *Acc. Chem. Res.* **2020**, 53, 852– 862.
41. Alfuth, J.; Jeannin, O.; Fourmigué, M. Topochemical, Single-Crystal-to-Single-Crystal [2+2] Photocycloadditions Driven by Chalcogen-Bonding Interactions. *Angew. Chem., Int. Ed.* **2022**, 61, e202206249.

42. Liu, J.; Han, X. J.; Han, N.; Li, B.; Sun, Y.; Wang, M.; Wu, G. One-Pot 'Click' Synthesis of Ring-in-Rings Complexes with Customizable π-Stacked Dyads. *J. Am. Chem. Soc.* **2025**, 147, 15838– 15846.
43. Jiang, Q.; Zhan, W.; Liu, X.; Bai, L.; Wang, M.; Xu, Y.; Liang, G. Assembly Drives Regioselective Azide-Alkyne Cycloaddition Reaction. *Nat. Commun.* **2023**, 14, 3935.
44. Ji, J.; Wei, X.; Wu, W.; Fan, C.; Zhou, D.; Kanagaraj, K.; Cheng, G.; Luo, K.; Meng, X.-G.; Yang, C. The More the Slower: Self-Inhibition in Supramolecular Chirality Induction, Memory, Erasure, and Reversion. *J. Am. Chem. Soc.* **2022**, 144, 1455– 1463.
45. Zhang, L.; Wang, H.; Li, S.; Liu, M. Supramolecular chiroptical switches. *Chem. Soc. Rev.* **2020**, 49, 9095– 9120.
46. Sun, H.; Yu, Z.; Li, C.; Zhang, M.; Shen, S.; Li, M.; Liu, M.; Li, Z.; Wu, D.; Zhu, L. Single-Luminophore Molecular Engineering for Rapidly Phototunable Solid-State Luminescence. *Angew. Chem. Int. Ed.* **2024**, 64, e202413827.
47. Wang, F.; Gan, F.; Shen, C.; Qiu, H. Amplifiable Symmetry Breaking in Aggregates of Vibrating Helical Molecules. *J. Am. Chem. Soc.* **2020**, 142, 16167– 16172.
48. Wu, B.; Wu, H.; Zhou, Y.; Zheng, D.; Jia, X.; Fang, L.; Zhu, L. Controlling Ultra-Large Optical Asymmetry in Amorphous Molecular Aggregations. *Angew. Chem., Int. Ed.* **2021**, 60, 3672– 3678.
49. Feng, X.; Wang, X.; Redshaw, C.; Tang, B. Z. Aggregation Behaviour of Pyrene-based Luminescent Materials, from Molecular Design and Optical Properties to Application. *Chem. Soc. Rev.* 2023, 52, 6715– 6753.
50. Balamut, B.; Hughes, R. P.; Aprahamian, I. Tuning the Properties of Hydrazone/Isosorbide-Based Switchable Chiral Dopants. *J. Am. Chem. Soc.* **2024**, 146, 24561– 24569.
51. Wang, H.; Bisoyi, H. K.; Urbas, A. M.; Bunning, T. J.; Li, Q. Reversible Circularly Polarized Reflection in a Self-Organized Helical Superstructure Enabled by a Visible-Light-Driven Axially Chiral Molecular Switch. *J. Am. Chem. Soc.* **2019**, 141, 8078– 8082.
52. Nie, F.; Yan, D. Bio-Sourced Flexible Supramolecular Glasses for Dynamic and Full-Color

Phosphorescence. *Nat. Commun.* **2024**, 15, 9491.

53. Garain, S.; Shoyama, K.; Ginder, L.-M.; Sárosi, M.; Würthner, F. The Delayed Box: Biphenyl Bisimide Cyclophane, a Supramolecular Nano-environment for the Efficient Generation of Delayed Fluorescence. *J. Am. Chem. Soc.* **2024**, 146, 22056– 22063.
54. Hu, F.; Hao, W.; Mücke, D.; Pan, Q.; Li, Z.; Qi, H.; Zhao, Y. Highly Efficient Preparation of Single-Layer Two-Dimensional Polymer Obtained from Single-Crystal to Single-Crystal Synthesis. *J. Am. Chem. Soc.* **2021**, 143, 5636– 5642.
55. Itoh, T.; Nomura, S.; Nakasho, H.; Uno, T.; Kubo, M.; Tohnai, N.; Miyata, M. Halogen Bond Effect for Single-Crystal-to-Single-Crystal Transformation: Topochemical Polymerization of Substituted Quinodimethane. *Macromolecules* **2015**, 48, 5450– 5455.
56. Li, L.; Jiang, P.; Zhang, X.; Li, Y. Sign Inversion of Circularly Polarized Luminescence in Cholesteric Liquid Crystals Induced by Mercury Ions through Binaphthyl Dopants' Conjugation Control. *Angew. Chem., Int. Ed.* **2025**, 64, e202417149.
57. Fu, R.; Zhao, Q.; Han, H.; Li, W.; Chen, F.; Tang, C.; Zhang, W.; Guo, S.; Li, D.; Geng, W.; Guo, D.; Cai, K. A Chiral Emissive Conjugated Corral for High-Affinity and Highly Enantioselective Recognition in Water. *Angew. Chem., Int. Ed.* **2023**, 62, e202315990.
58. Ong, W. Swager, T. Dynamic self-correcting nucleophilic aromatic substitution. *Nat. Chem.* **2018**, 10, 1023– 1030.
59. Sato, Y.; Abekura, M.; Oriki, T.; Nagashima, Y.; Uekusa, H.; Tanaka, K. Shape- and Size-Tunable Synthesis of Covalent Organic Cages through Rh-Catalyzed Regioselective [2+2+2] Cycloaddition. *Angew. Chem., Int. Ed.* **2023**, 62, e202304041.
60. Dayanara, N. L.; Froelich, J.; Roomea, P.; Perrin, D. M. Chemoselective, Regioselective, and Positionally Selective Fluorogenic Stapling of Unprotected Peptides for Cellular Uptake and Direct Cell Imaging. *Chem. Sci.* **2025**, 16, 584– 595.
61. Chrzastek, A.; Thanasi, I.; Irving, J.; Chudasama, V.; Baker, J. Dual Reactivity Disulfide Bridging Reagents; Enabling New Approaches to Antibody Fragment Bioconjugation. *Chem. Sci.* **2022**, 13, 11533– 11539.

62. Zhou, P.; Xing, R.; Li, Q.; Li, J.; Yuan, C.; Yan, X. Steering Phase-Separated Droplets to Control Fibrillar Network Evolution of Supramolecular Peptide Hydrogels. *Matter* **2023**, 6, 1945–1963.
63. Kai, U.; Sumida, R.; Tanaka, Y.; Yoshizawa, M. Discrimination of Perfluorinated Arenes/Alkanes by Modulable Polyaromatic Capsules. *J. Am. Chem. Soc.* **2025**, 147, 10640–10646.
64. Huang, Z.; Chen, X.; Wu, G.; Metrangolo, P.; Whitaker, D.; McCune, J.; Scherman, O. Host-Enhanced Phenyl-Perfluorophenyl Polar−π Interactions. *J. Am. Chem. Soc.* **2020**, 142, 7356–7361.
65. Lu, T.; Chen, F. Multiwfn: A Multifunctional Wavefunction Analyzer. *J. Comput. Chem.* **2012**, 33, 580– 592.

Acknowledgements

This works is also supported by the National Natural Science Foundation of China (Nos.22171165, 22371170, 22571184) and National Natural Science Foundation of Shandong Province (ZR2025QA15).

Author contributions

Z.W. and C.C. contributed equally to this work. Z.W. and P.X. proposed the project. Z.W. performed morphology characterization and DFT simulations; C.C. carried out compound synthesis, spectroscopic measurements and related experiments. A.H. and P.X. supervised the research. P.X. wrote the manuscript. All authors discussed the results and reviewed the manuscript.

Competing interests

The authors declare no competing interests.

Editorial Summary

Controlled reactions in solid or self-assembled states underpin dynamic materials and topochemical processes but suffer reduced efficiency without diffusion. Here, the authors report that an aromatic cystine derivative undergoes multiple topochemical steps with strong templating and chiral inheritance.

Peer review information: *Nature Communications* thanks Chun-Sen Liu and the other, anonymous, reviewers for their contribution to the peer review of this work. A peer review file is available.